


 Cite this: *Lab Chip*, 2020, 20, 3036

## Quantitative design strategies for fine control of oxygen in microfluidic systems†

 Venktesh S. Shirure,<sup>‡</sup><sup>a</sup> Sandra F. Lam,<sup>‡</sup><sup>b</sup> Bhupinder Shergill,<sup>a</sup> Yunli E. Chu,<sup>b</sup> Natalie R. Ng<sup>‡</sup><sup>b</sup> and Steven C. George<sup>\*a</sup>

Hypoxia, or low oxygen (O<sub>2</sub>) tension, is a central feature of important disease processes including wound healing and cancer. Subtle temporal and spatial variations (≤1% change) in the concentration of O<sub>2</sub> can profoundly impact gene expression and cellular functions. Sodium sulfite reacts rapidly with O<sub>2</sub> and can be used to lower the O<sub>2</sub> concentrations in PDMS-based tissue culture systems without exposing the cell culture to the chemical reaction. By carefully considering the mass transfer and reaction kinetics of sodium sulfite and O<sub>2</sub>, we developed a flexible theoretical framework to design an experimental microfluidic system that provides fine spatial and temporal control of O<sub>2</sub> tension. The framework packages the dimensions, fluid flow, reaction rates, concentrations, and material properties of the fluidic lines and device into dimensionless groups that facilitate scaling and design. We validated the theoretical results by experimentally measuring O<sub>2</sub> tension throughout the experimental system using phosphorescence lifetime imaging. We then tested the system by examining the impact of hypoxia inducible factor-1α (HIF-1α) on the proliferation and migration of MDA-MB-231 breast cancer cells. Using this system, we demonstrate that mild constant hypoxia (≤4%) induces HIF-1α mediated functional changes in the tumor cells. Furthermore, slow (>12 hours), but not rapid (<1 hour), fluctuations in O<sub>2</sub> tension impact HIF-1α mediated proliferation and migration. Our results provide a generalized framework for fine temporal and spatial control of O<sub>2</sub> and emphasize the need to consider mild spatial and temporal changes in O<sub>2</sub> tension as potentially important factors in disease processes such as cancer.

 Received 6th April 2020,  
Accepted 15th July 2020

DOI: 10.1039/d0lc00350f

rsc.li/loc

## Introduction

Hypoxia is generally considered to be O<sub>2</sub> tension <5% and occurs *in vivo* when O<sub>2</sub> diffusing from the local vascular network is insufficient to meet the needs of the tissue due to increased metabolic demand or reduced supply. Hypoxia changes the expression of a plethora of genes in cells that impact migration, proliferation, and metabolism. These alterations can impact important disease processes such as cancer, including tumor angiogenesis, cancer stem cell maintenance, dormancy, and immune evasion, all of which contribute to tumor progression and treatment resistance.<sup>1,2</sup> The response to hypoxia is primarily controlled by the transcription factor hypoxia-inducible factor 1 (HIF-1)<sup>3,4</sup> through its two subunits (HIF-1α and HIF-1β). HIF-1α is

degraded by a family of prolyl hydroxylases under physioxic (mean tissue O<sub>2</sub> of ~5%) conditions, but during hypoxic conditions, the action of the prolyl hydroxylases is compromised leading to increased levels of HIF-1α.<sup>1</sup> Interestingly, the accumulation of HIF-1α increases non-linearly with decreasing O<sub>2</sub> concentrations,<sup>5</sup> providing a robust mechanism to counter progressively lower O<sub>2</sub> levels. Thus, a subtle reduction (≤1% change) in the concentration of O<sub>2</sub> can potentially impact gene expression and cellular function. Each individual cell in a tissue could be exposed to small differences in the concentration of O<sub>2</sub>. For example, in an *in vivo* tumor microenvironment (TME), the O<sub>2</sub> tension drops within a few millimeters from physioxia near the periphery of the tumor to near zero at the core of a necrotic tumor. Additionally, the blood supply to the tumor tissue fluctuates due to the irregular and leaky vasculature. As such, the cells in the TME are exposed to heterogenous O<sub>2</sub> concentrations in both space and time.<sup>6,7</sup> Finely controlling the O<sub>2</sub> concentration both spatially and temporally will allow us to leverage the non-linear response of HIF-1α.

Organ-on-a-chip microfluidic systems provide an *in vitro* 3D physiologic alternative to *in vivo* biological studies. Several systems have been designed to create hypoxia in 3D cell culture

<sup>a</sup> Department of Biomedical Engineering, University of California Davis, CA, USA.  
E-mail: scgeorge@ucdavis.edu

<sup>b</sup> Department of Biomedical Engineering, Washington University in St. Louis, MO, USA

† Electronic supplementary information (ESI) available. See DOI: 10.1039/d0lc00350f

‡ These authors contributed equally to the manuscript.

models.<sup>8–10</sup> Using inert gases to lower O<sub>2</sub> concentrations<sup>8–10</sup> can lead to bubble formation and evaporation of fluids, while other methodologies that employ water with defined O<sub>2</sub> requires gas exchangers and airtight systems<sup>10,11</sup> making them impractical for routine long-term experiments. We have previously demonstrated in principle that the reaction between aqueous sodium sulfite and O<sub>2</sub> can be utilized to create O<sub>2</sub> gradients in microfluidic devices.<sup>12</sup> This method does not expose the cell cultures to exogenous O<sub>2</sub> scavenging chemicals to lower oxygen tension and only requires inert O<sub>2</sub> sensing dyes when measuring the O<sub>2</sub> concentration in the culture. Nonetheless, as a small molecule, O<sub>2</sub> is pervasive and promiscuous, and thus creates hurdles to finely ( $\leq 1\%$  change in O<sub>2</sub>) modulate the local levels of O<sub>2</sub>. A precise and detailed engineering design that considers mass transport of O<sub>2</sub> from the environment and the kinetics of scavenging can potentially overcome these challenges.

In this study, we provide a generalized, and thus flexible, mathematical and experimental framework for creating precise and fine spatiotemporal control of O<sub>2</sub> tension in a microfluidic system that can be applied to a wide range of polymer-based microfluidic devices. We consider mass transfer and reaction kinetics throughout an entire typical experimental system, which is composed of a syringe pump, tubing, and incubator, as well as the microfluidic device itself. We validated theoretical results by experimentally measuring O<sub>2</sub> tension throughout the system using phosphorescence lifetime imaging. Furthermore, we tested the HIF-1 $\alpha$ -mediated response of tumor cells to mild and intermittent hypoxia and demonstrate significant phenotypic responses to subtle variations in O<sub>2</sub> concentrations in both space and time.

## Materials and methods

### Microfluidic device design and microfabrication

We used a three-tissue-chambered microfluidic device described in more detail in our previous study.<sup>12</sup> The central compartment is the largest with a volume of  $\sim 60$  nL; the adjacent compartments are slightly smaller, each with a volume of  $\sim 20$  nL. The central compartment was filled with a cell-free fibrin gel and the adjacent compartments with cells mixed in fibrin gel (Fig. 1A and B). The two separate cell chambers allow study of hypoxia and physioxia conditions in the same device. Media lines connect to the central chamber to feed all three chambers. The 100  $\mu\text{m}$  wide microfluidic lines run parallel to the cell compartments and are used to introduce the O<sub>2</sub> scavenger or incubator O<sub>2</sub> (5%) in close proximity to the chambers. These microfluidic lines are separated by a 30  $\mu\text{m}$  wall from the cell compartments.

Microfabrication of the device was performed using standard soft lithography. Briefly, a master mold of 100  $\mu\text{m}$  height was prepared using SU-8 3050 (MicroChem, Newton, MA). The mold was silanized, polydimethylsiloxane (PDMS; Dow Corning, Elizabethtown, KY) was prepared by using 10 : 1 ratio of elastomer to curing agent, and was then poured

over the mold, and allowed to cure at 65 °C for at least two hours. The PDMS was peeled off, the inlets and outlets were punched out of the device, and a glass slide was bonded to the device using plasma treatment. The device was placed in a 120 °C oven for a minimum of 15 min and sterilized for 1 hour using UV light before experimentation.

### Sodium sulfite loading

The experimental set up for pumping sodium sulfite (Fig. 1C) consisted of a 20 mL syringe connected to the microfluidic device *via* a 23G stainless-steel needle (length = 12.5 mm, nominal ID = 0.406 mm, and OD = 0.7 mm; Jensen Global, North Andover, MA) and a Tygon tubing (length = 1524 mm, ID = 0.508 mm and OD = 1.524 mm; Saint-Gobain, Valley Forge, PA). The syringe body is made up of polypropylene which has a very low permeability for O<sub>2</sub> (three orders of magnitude less than PDMS<sup>13,14</sup>) and therefore, provides a nearly complete barrier to O<sub>2</sub> transport. The 0.5 M sodium sulfite solution was first prepared by dissolving sodium sulfite (Sigma-Aldrich, St. Louis, MO) into deionized water and warming the solution to 37 °C. This solution was appropriately diluted in deionized water to the desired concentration and immediately suctioned into the syringe. A Tygon tube, connected to the scavenger line of the microfluidic device, was quickly attached to the syringe using the needle. The syringe was installed on a syringe pump, and the solution flowed at 200 nL s<sup>-1</sup>. In the chronic hypoxia condition, we perfused 1, 2, 3, or 5 mM concentrations of sodium sulfite continuously for 5 additional days. For intermittent hypoxia study, 3 or 9 mM sodium sulfite solutions flowed in cycles of 24 or 2 hours, respectively for 5 additional days.

### Phosphorescence lifetime imaging microscopy (PhLIM)

To measure O<sub>2</sub> inside the microfluidic device, we used PhLIM, a detailed protocol for which has been previously published.<sup>12,15</sup> Briefly, the Oxyphor G4 (O<sub>2</sub> Enterprises, Philadelphia, PA) dye was excited with a 635 nm laser modulated at 10 kHz with 5% duty cycle in an FV1200 confocal microscope (Olympus) with phosphorescent lifetime instrumental upgrade from ISS (Urbana-Champaign, IL). A miniTDU equipped with two Hamamatsu 7422p-50 detectors was coupled directly to the confocal head for emission beam collection. For O<sub>2</sub> and temperature control, an Okolab's stage-top incubator with custom microenvironment chamber (Okolab, San Bruno, CA) was installed to the confocal microscope.

To estimate O<sub>2</sub> concentrations, we correlated the lifetime of Oxyphor G4 dye with known O<sub>2</sub> concentrations in the microfluidic device at 37 °C. The devices were loaded with fibrin and Oxyphor G4 prepared at 20  $\mu\text{M}$  and were equilibrated with the stage incubator for at least 90 min. A total of five repeat frames were acquired and averaged. This data was then used with manufacturer recommended equations to generate a calibration curve. To measure O<sub>2</sub> for

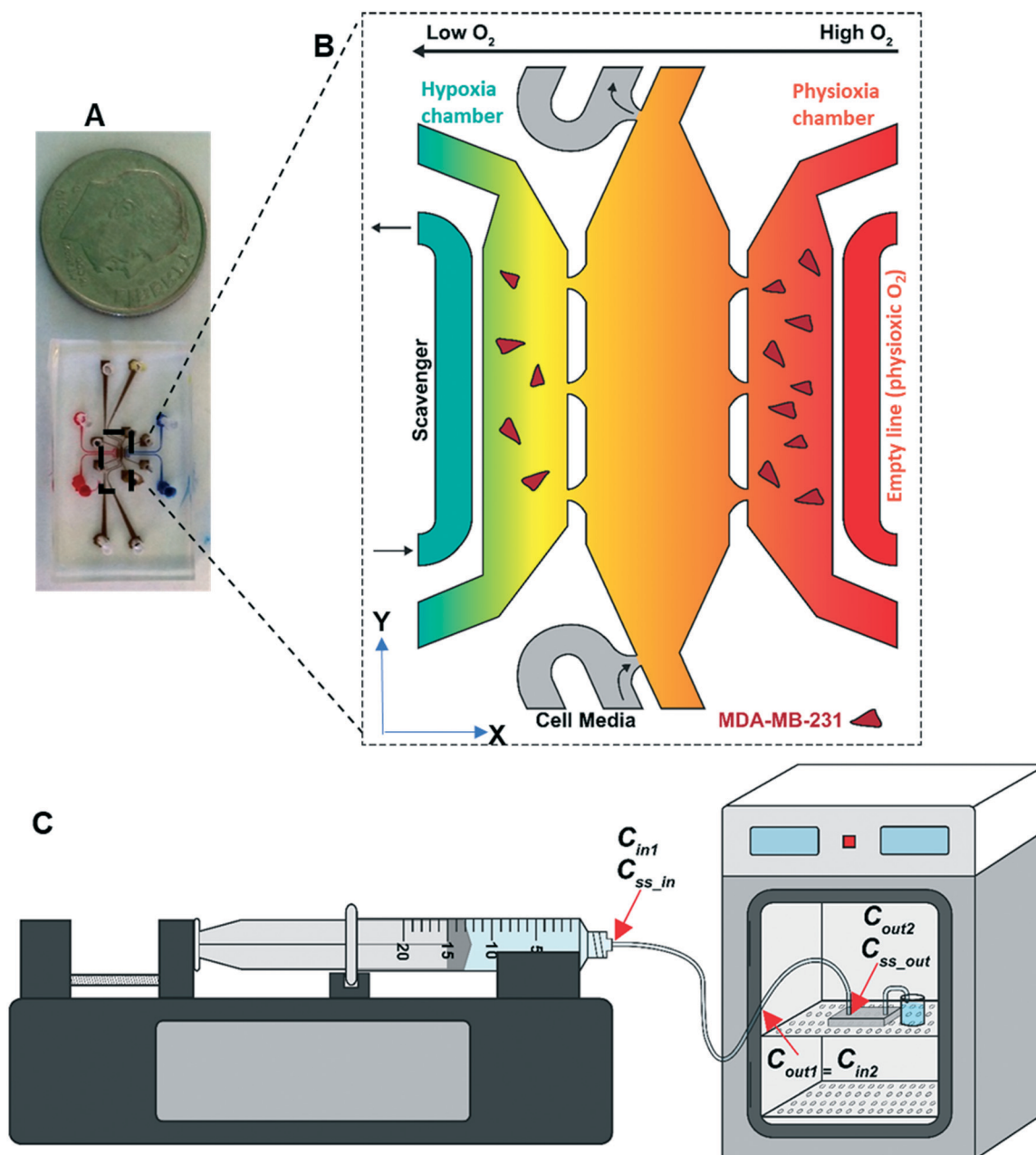


**Fig. 1** Schematics of the microfluidic device and the experimental set up. (A) The microfluidic device at low magnification; it is about the size of a US dime (left image). (B) The device consists of three tissue chambers and four fluidic lines. The outer tissue chambers are loaded with MDA-MB-231 cells in a fibrin gel, and the central chamber is loaded with plain fibrin. The tissues are fed through the fluidic lines (grey) attached to the central chambers. The scavenger (sodium sulfite) is convected through the scavenger line (green), while the opposite fluidic line (red) is left empty and open to the  $O_2$  tension in the incubator (5% in our experiments). The increasing intensity of red indicates increasing  $O_2$ . (C) Experimental set up for perfusing sodium sulfite through the microfluidic chip consists of a syringe installed on a syringe pump, tubing (Tygon), part of which is outside and the other part is inside the cell culture incubator, and the microfluidic chip inside the incubator. The concentrations of  $O_2$  at the inlet ( $C_{in1}$ ), at the interface with incubator ( $C_{out1} = C_{in2}$ ), and at the outlet ( $C_{out2}$ ), and the concentration of sodium sulfite at the inlet ( $C_{ss\_in}$ ) and outlet ( $C_{ss\_out}$ ) of the tubing are indicated.

various sodium sulfite conditions, devices loaded with fibrin and Oxyphor G4 in the tissue chambers were pumped with desired concentration of sodium sulfite for 24 hours. The phosphorescent lifetime of each pixel was then recorded and converted to %  $O_2$  using the calibration curve, thus creating a 2D map of  $O_2$  concentrations.

#### Generalized framework for controlling $O_2$ tension in the tubing leading to the microfluidic device

Given the high concentration of ambient  $O_2$  (20%), the relatively rapid rate of diffusion in the gas phase, and consumption of  $O_2$  by sodium sulfite, it is imperative to

characterize the O<sub>2</sub> tension in all compartments of the experimental system including the syringe, tubing outside the incubator, tubing inside the incubator, and the microfluidic device itself (Fig. 1C). The design of each of these compartments can then potentially play an important role in creating the desired spatial and temporal O<sub>2</sub> tension profiles within the tissue or cellular microenvironment.

The first step was to examine the O<sub>2</sub> tension in the syringe installed on the pump. We determined that if the time course of a study exceeds four hours, and sodium sulfite concentration exceeds 0.27 mM, at room temperature, the concentration of O<sub>2</sub> in the syringe can be assumed to be zero based on our measured kinetic rate constant (Fig. S1 and S2†). Under this condition, the steady state concentration of sodium sulfite in the syringe is the starting concentration minus that consumed by O<sub>2</sub> to reach a zero O<sub>2</sub> concentration, or 0.54 mM (eqn (S1)†). Finally, the syringe with a needle is insulated from all sides, except the outlet. For  $Q > 1 \text{ nL s}^{-1}$  (typical low range for nanoliter syringe pumps), we can neglect back diffusion of O<sub>2</sub> from the tubing into the syringe (see analysis in ESI†).

The next step was to model the flow of sodium sulfite through the tubing. A simple mass balance on the tube (see ESI† eqn (S2)) can be solved to produce the following relationships for the sodium sulfite concentration at the outlet of the tubing,  $C_{\text{ss\_out}}$ , and the residence time in the tube,  $\tau$  (s):

$$C_{\text{ss\_out}} = (C_{\text{ss\_in}}^{0.35} - 0.7 \tau K)^{\frac{1}{0.35}} \quad (1)$$

$$\tau = \frac{\pi r^2 L}{Q} \quad (2)$$

where  $C_{\text{ss\_in}}$  (mM) is the concentration of sodium sulfite at the inlet of the tube (Fig. 1C). The concentration of sodium sulfite was assumed in excess (>1 mM) and thus constant along the length of tube (this for a mean residence time in tube <2000 s, see analysis and Fig. S3 in the ESI†). The sodium sulfite concentration is denoted  $C_{\text{ss}}$  in the rest of the analysis.

The next step invoked classical theory of mass transfer with reaction to model convective transport of fluid through a cylindrical tube (the Tygon tubing) with a semi-permeable wall to O<sub>2</sub>. The radius of the tube was small compared to the length, so the concentration of O<sub>2</sub> was assumed to vary only along the length of the tube. The one-dimensional convection-diffusion equation was then solved to determine the outlet concentration of O<sub>2</sub> from a generic tube,

$$C_{\text{out}}^{\circ} = C_{\text{in}}^{\circ} e^{-\frac{1}{\text{Pe}}} + (y_{\text{A}} - \text{Da}) \left(1 - e^{-\frac{1}{\text{Pe}}}\right) \quad (3)$$

where

$$C_{\text{out}}^{\circ} = \frac{C_{\text{out}}}{S_{\text{w}}}; C_{\text{in}}^{\circ} = \frac{C_{\text{in}}}{S_{\text{w}}}; \text{Pe} = \frac{Q}{2\pi r L P_{\text{m}}} \text{ and } \text{Da} = \frac{K C_{\text{ss}}^{0.65} r}{2 S_{\text{w}} P_{\text{m}}} \quad (4)$$

$C_{\text{in}}^{\circ}$  and  $C_{\text{out}}^{\circ}$  are the fractional concentrations and  $C_{\text{in}}$  (mM) and  $C_{\text{out}}$  (mM) are the molar concentrations of O<sub>2</sub> at the inlet

and outlet of the tube, respectively; Da is Damkohler number, Pe is the Peclet number,  $y_{\text{A}}$  is the partial pressure of O<sub>2</sub> in air,  $Q$  ( $\text{m}^3 \text{ s}^{-1}$ ) is the volumetric flow rate of sodium sulfite solution;  $r$  (m),  $L$  (m), and  $P_{\text{m}}$  ( $\text{m s}^{-1}$ ) are the radius, length, and permeability ( $6.30 \pm 0.03 \times 10^{-8} \text{ m s}^{-1}$ , see Fig. S4 and analysis in ESI†) of the tube, respectively;  $C_{\text{ss}}$  (mM) is the concentration of sodium sulfite, and  $S_{\text{w}}$  (mM) is the solubility of O<sub>2</sub> in water.

In our experiment, a part of the Tygon tubing was outside the incubator (Fig. 1C) and thus at a different temperature. Eqn (4) can be modified with the subscripts 1 and 2 denoting properties for those parts outside and inside the incubator (Fig. 1C), respectively.

$$C_{\text{out1}}^{\circ} = \frac{C_{\text{out1}}}{S_{\text{w1}}}; C_{\text{in1}}^{\circ} = \frac{C_{\text{in1}}}{S_{\text{w1}}}; \text{Pe}_1 = \frac{Q}{2\pi r L_1 P_{\text{m}}}; \text{Da}_1 = \frac{K C_{\text{ss}}^{0.65} r}{2 S_{\text{w1}} P_{\text{m}}} \quad (5)$$

$$C_{\text{out2}}^{\circ} = \frac{C_{\text{out2}}}{S_{\text{w2}}}; C_{\text{in2}}^{\circ} = \frac{C_{\text{in2}}}{S_{\text{w2}}}; \text{Pe}_2 = \frac{Q}{2\pi r L_2 P_{\text{m}}}; \text{Da}_2 = \frac{K C_{\text{ss}}^{0.65} r}{2 S_{\text{w2}} P_{\text{m}}} \quad (6)$$

eqn (6) can be written using eqn (5) as follows

$$\text{Pe}_2 = \text{Pe}_1 L^{\circ}; \text{Da}_2 = \text{Da}_1 S_{\text{w}}^{\circ}; L^{\circ} = \frac{L_1}{L_2} \quad (7)$$

where

$$S_{\text{w}}^{\circ} = \frac{S_{\text{w1}}}{S_{\text{w2}}} (\text{constant}) \quad (8)$$

Since the tube is continuous,

$$C_{\text{in2}} = C_{\text{out1}} \text{ or } C_{\text{in2}}^{\circ} = C_{\text{out1}}^{\circ} S_{\text{w}}^{\circ} \quad (9)$$

$C_{\text{out1}}^{\circ}$  can be calculated from eqn (3) using the definitions provided in eqn (5). The outlet concentration of the tube ( $C_{\text{out2}}^{\circ}$ ), which is the concentration of fluid that enters the microfluidic device, can then be calculated from eqn (3) using definitions in eqn (6) and (9).

The O<sub>2</sub> concentration at the outlet of the tubing ( $C_{\text{out2}}$ ), also the inlet concentration to the microfluidic device, thus depends on the following independent parameters:  $Q$ ,  $r$ ,  $L_1$ ,  $L_2$ ,  $P_{\text{m}}$ ,  $C_{\text{ss}}$ ,  $S_{\text{w1}}$ ,  $S_{\text{w2}}$ ,  $y_{\text{A1}}$ ,  $y_{\text{A2}}$ . Among these parameters,  $S_{\text{w1}}$ ,  $S_{\text{w2}}$ ,  $y_{\text{A1}}$ , and  $y_{\text{A2}}$ , are constants for the experimental system. The variable parameters are grouped into three independent dimensionless numbers (eqn (7)): Peclet number ( $\text{Pe}_1$ ), Damkohler number ( $\text{Da}_1$ ), and the ratio of lengths ( $L^{\circ}$ ), which completely define the tubing and can provide a convenient way to analyze, and thus design, this part of the system (Table 1).

### Generalized framework for controlling O<sub>2</sub> tension in the microfluidic device

We used the  $C_{\text{out2}}$  as the inlet boundary condition ( $C_{\text{in3}}$ ) for a simple single microfluidic channel (Fig. 2B) to develop a design equation for the device. The dimensions of the channel ( $W_3$ ,  $H_3$ , and  $L_3$ ), the flow rate ( $Q$ ), and  $C_{\text{ss}}$  were varied within a range that is typically used for organ-on-chip devices (Table 3), and the O<sub>2</sub> profiles in the device were

**Table 1** The parameters used to solve eqn (1)–(9) to create Fig. 2A

Notation	Description	Value
$P_m$	Permeability of tubing	$6.3 \times 10^{-8} \text{ m s}^{-1}$
$y_{A1}$	Fractional $O_2$ in air	0.2095
$y_{A2}$	Fractional $O_2$ in the incubator	0.05
$S_{w1}$	Solubility of pure $O_2$ at 1 atm, 22 °C	1.35 mM
$S_{w2}$	Solubility of pure $O_2$ at 1 atm, 37 °C	1.05 mM
$r$	Radius of the tubing	0.25 mm
$L_1$	Length of tubing outside incubator	0.91 m
$L_2$	Length of tubing outside incubator	0.61 m
$K$	Reaction rate constant	$3 \times 10^{-5} \text{ mM}^{0.35} \text{ s}^{-1}$
$C_{ss\_in}$	Concentration of sodium sulfite at the inlet of the tubing	1–7 mM
$n$	Order of the scavenging reaction	0.65
$Q$	Flow rate through the tubing	0–50 $\mu\text{L min}^{-1}$
$L^\circ$	Ratio of length of tubing outside to inside incubator	0.5–2.5

computed using COMSOL (see below). The relevant non-dimensional numbers ( $Pe_3$ ,  $Da_3$ , and  $C_{in3}^\circ$ ), are similar to that used in the tubing analysis, and were defined as follows,

$$Pe_3 = \frac{\left(\frac{L_3}{\tau_3}\right)}{D_w \left(\frac{A_3}{V_3}\right)} = \frac{Q}{2(W_3 + H_3)D_w}; \quad Da_3 = \frac{2KC_{ss}^{0.65}(W_3 + H_3)L_3}{S_{w2}D_w} \quad (10)$$

where the suffix 3 denotes dimensions and properties associated with the microfluidic channel.  $A_3$  and  $V_3$  are the surface area and the volume of the channel.

### Finite element modeling of the device

To analyze  $O_2$  transport within the microfluidic device, 3D designs of the microfluidic devices (Fig. 1A and 2B) were simulated in COMSOL Multiphysics 5.2a (Burlington, MA). A PDMS block ( $35 \times 25 \times 5 \text{ mm}^3$ ) housed the 100  $\mu\text{m}$  tall channels. The bottom of the channels and PDMS were bonded to the glass (see microfluidic design for more details). Fluid flow was modeled using the transport through porous media or laminar flow module with a no-slip boundary condition at the walls. The hydrostatic pressure difference drove fluid through the tissue, and a pump drove the sodium sulfite solution through the scavenger line at a defined velocity (Table 2). The  $O_2$  transport through PDMS was modeled using the transport of diluted species module. The following assumptions were made: 1) PDMS–air interface was in equilibrium; 2) the concentration of  $O_2$  at the interfaces obeys Henry's law; 3) glass was assumed to be impermeable to  $O_2$ ; and 4) the inlet concentration of  $O_2$  in the fluid feeding the tissues was equal to the solubility of the  $O_2$  in water at the  $O_2$  partial pressure in the incubator (5% for our study). The PDMS–media interface was modeled using a pointwise constraint at the boundary by the stiff-spring method.<sup>12</sup> The mass transfer through the tissue was performed by coupling the transport through porous media module with the transport of diluted species module. Michaelis–Menten kinetics were used to model the

consumption of  $O_2$  via cellular metabolism<sup>12,16</sup> with the following rate equation

$$R = \rho_{\text{cell}} \frac{V_{\text{max}} C}{K_m + C}$$

where  $V_{\text{max}}$  (mol per cell per s) is the maximum rate of oxygen consumption per cell,  $K_m$  (mol  $\text{m}^{-3}$ ) is the concentration of oxygen at which the oxygen consumption rate is half that of  $V_{\text{max}}$ ,  $C$  is oxygen concentration and  $\rho_{\text{cell}}$  (cells per  $\text{m}^3$ ) is the volumetric cell density. The cells were assumed uniformly distributed throughout the tissue chamber.

The consumption of  $O_2$  through the sodium sulfite reaction was modeled using the reaction rate constant measured in this study. The concentration at the inlet of the tubing and found by using eqn (3)–(9). For the intermittent hypoxia studies, the velocity at the inlet of the scavenger line was loaded with periodic velocities of 0 or 200  $\text{nL s}^{-1}$  with cycle times of 2 or 24 hours. This was modeled using a piecewise periodic function that has continuous second derivative smoothing and the relative size of the transition zone was 0.1. The system properties used in this model are given in Table 2. The parameters varied for the device with a single microfluidic line (Fig. 2B) are given in Table 3.

### Cell culture and shRNA treatments

MDA-MB-231 breast cancer cells constitutively expressing fluorescent protein, MCherry (Cell Biolabs, Inc; San Diego, CA) were grown in Dulbecco's modified Eagle medium (DMEM, ThermoFisher, Waltham, MA) containing 10% fetal bovine serum (FBS, Sigma-Aldrich, St. Louis, MO), 1% L-glutamine (ThermoFisher), and 1% penicillin–streptomycin (ThermoFisher). The cells were transduced with HIF-1 $\alpha$  shRNA particles to knockdown the expression of HIF-1 $\alpha$  gene and a scrambled shRNA particle served as a negative control. For the cell transduction, MDA-MB-231 seeded in a 24-well plate at  $4.5 \times 10^4$  cells per well and allowed to grow overnight to about 50% confluency. A 250  $\mu\text{L}$  media solution containing 5  $\mu\text{g mL}^{-1}$  polybrene (Santa Cruz Biotechnology) was added dropwise to each well. Next, shHIF-1 $\alpha$  or scrambled lentiviral particles (Santa Cruz Biotechnology, Dallas, TX),<sup>17–19</sup> were diluted in cell culture media at 1:50 (v/v) (MOI = 1 to a volume of 250  $\mu\text{L}$ ) and incubated for 18 hours. The clones were selected by using 3  $\mu\text{g mL}^{-1}$  of puromycin dihydrochloride (Santa Cruz).

### qRT-PCR and immunofluorescence staining

qRT-PCR was performed following standard methodology. Briefly, RNA was extracted and purified using the RNeasy Plus Mini Kit (Qiagen, Venlo, Netherlands) and converted to cDNA using a reverse transcription kit (Applied Biosystems). TaqMan Gene Expression Assays (HIF-1 $\alpha$ : Hs00154153\_m1, 18S: Hs99999901\_s1) and CFX96 Real-Time PCR Detection

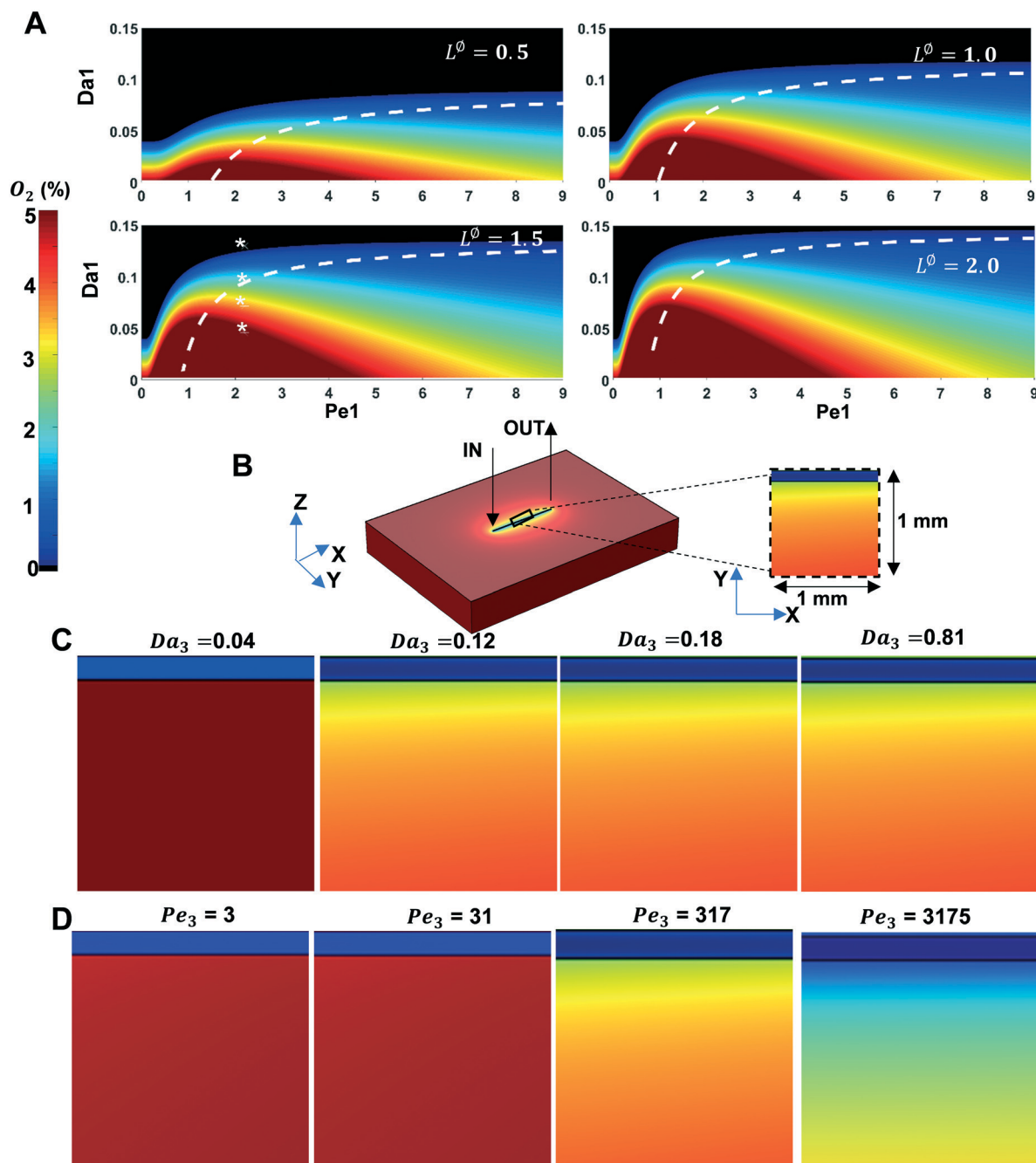


**Fig. 2** The  $O_2$  profiles at the outlet of tubing and within a simple microfluidic chip found by computational models. (A) The concentration of  $O_2$  ( $C_{out2}$ ) at the outlet of the tubing was computed using eqn (1), (2) and (5)–(9) at various  $Pe_1$ ,  $Da_1$ , and  $L^\phi$ . The white line indicates  $Pe_{crit}$  (eqn (11)). The \* indicates the  $C_{out2}$  for  $Da_1 = 0.05, 0.07, 0.09$ , and  $0.13$  ( $C_{ss} = 1, 2, 3$ , and  $5$  mM sodium sulfite concentrations). (B) Finite element simulations were performed on a device with a single microfluidic line with inlet and outlet for scavenger flow. The magnified insert shows the concentration profile in an  $X$ - $Y$  plane, the centre of which is  $5$  mm in  $X$ -direction from the inlet and at the vertical midpoint of the device height. The profiles at this plane are shown for (C)  $Pe_3 = 317$  and (D)  $Da_3 = 0.12$ .

System (Bio-Rad, Hercules, CA) was used to measure the expression levels. Relative HIF-1 $\alpha$  gene expression for control MDA-MB-231 (WT), scramble MDA-MB-231 (Scramble), and shRNA HIF-1 $\alpha$  MDA-MB-231 (shHIF-1 $\alpha$ ) were compared using the  $\Delta\Delta C_t$  method.

To perform immunofluorescence staining, we fixed the cells in a 10% formalin for 15 min, permeabilized with a

0.1% Tween in 0.5% Tris-buffered saline for 30 min and blocked with 2% BSA for 1 hour. The cells were incubated with anti-human rat HIF-1 $\alpha$  (ThermoFisher) mAb overnight, washed, and then incubated with Alexa Fluor 488-conjugated goat anti-rat IgG (Invitrogen) overnight. The cells were then washed, stained with DAPI, and imaged using an FV1200 Fluoview confocal laser scanning microscope (Olympus).

**Table 2** The values of parameters used in the finite simulations of the tissue chip (Fig. 3A and C and 6A and B)

Parameter	Value
Inlet pressure (high side)	19.0 mmH <sub>2</sub> O
Outlet pressure (high side)	18.5 mmH <sub>2</sub> O
Inlet pressure (low side)	18.5 mmH <sub>2</sub> O
Outlet pressure (low side)	18 mmH <sub>2</sub> O
Fibrin permeability	$1.5 \times 10^{-13} \text{ m}^2$
Diffusion of O <sub>2</sub> through PDMS	$3.55 \times 10^{-9} \text{ m}^2 \text{ s}^{-1}$
Diffusion of O <sub>2</sub> through water	$2.10 \times 10^{-9} \text{ m}^2 \text{ s}^{-1}$
Max rate of O <sub>2</sub> metabolism by cells ( $V_{\text{max}}$ )	$1.3 \times 10^{-17} \text{ mol s}^{-1}$
O <sub>2</sub> consumption at half of $V_{\text{max}}$ ( $K_M$ )	$8 \times 10^{-3} \text{ mol m}^{-3}$
Sodium sulfite reaction rate constant ( $K$ )	$3 \times 10^{-5} \text{ mM}^{0.35} \text{ s}^{-1}$
Order of the sodium sulfite reaction ( $n$ )	0.65
Partition coefficient of O <sub>2</sub> at 37 °C	0.14
Number of cells in each side chambers	$5 \times 10^6$
Flow rate of scavenger	$12 \mu\text{L min}^{-1}$

**Table 3** The parameters used for simulations (Fig. 2B–E) and for computing parameters in Table 4

Notation	Description	Values
$W$	Width of the channel	50, 100, 200, 400 $\mu\text{m}$
$H$	Height of the channel	50, 100, 200, 400 $\mu\text{m}$
$L$	Length of the channel	10 mm
$Q$	Flow rate	150 $\mu\text{L}$ per day–200 mL per day
$C_{\text{ss}}$	Concentration of sodium	1–2000 mM

### Experimental model of tumor growth and migration

To create a simple experimental model of tumor growth and migration, the central chamber was first loaded with fibrin, which is prepared by mixing fibrinogen (Sigma-Aldrich) 16 mg mL<sup>-1</sup> and 50 U mL<sup>-1</sup> thrombin and the device was incubated for 30 min at 37 °C. The adjacent chambers were loaded with MDA-MB-231 cells ( $5 \times 10^6$  cells per mL) in fibrin, and the device was incubated for 30 min, before perfusing media through the lines connected to the central chamber. The cell density used for the experimentation was chosen based on previous experience from our group with tumor cell lines in microfluidic devices.<sup>20</sup> We found that at about  $5 \times 10^6$  cells per mL, cells exhibit migration and proliferation and provide enough cells per field of view to capture sufficient events for the analysis. Higher concentrations can lead to degradation of the extracellular matrix (ECM). The devices were maintained in a 5% O<sub>2</sub> incubator. After 24 hours, a sodium sulfite solution was introduced through one of the microfluidic lines (Fig. 1B) in some devices for an additional 5 days.

We quantified two features of tumor progression in our study: 1) growth, and 2) migration. Fluorescent images of the microfluidic device were taken before hypoxia treatment and at the end of the experiment using an IX83 motorized epifluorescence microscope (Olympus, Tokyo, Japan). Each image was cropped to isolate the fluorescent area in the left, central, or right chamber, and the images were randomized

and analyzed for tumor area using ImageJ. The starting cell concentrations in the devices vary due to variability in cell loading, which originates from small changes in quantifying cell concentrations prior to loading. Therefore, we chose to normalize each experiment by the starting cell concentration. Thus, tumor growth (fold) was defined as the fluorescent tumor area in the left or right chamber on the final day divided by the area in the same chamber on day 1 of the experiment. Tumor cell migration was quantified by dividing the tumor area in the central chamber by the total tumor area in the left, central, and right chamber on the final day of the experiment.

### Statistical analysis

The results are represented as mean  $\pm$  SD for 3–6 biological replicates. A data point was considered an outlier if it was more than 1.5 IQR (interquartile range) above the third quartile or 1.5 IQR below the first quartile and excluded from analysis. A Mann–Whitney test was applied to compare tumor growth in the left and right chambers or migration parameter among shHIF-1 $\alpha$ , WT, or Scramble cells. Statistical significance was considered at the  $p < 0.05$  level, and GraphPad Prism 6 was used for data analysis.

## Results

### Generalized quantitative design strategy for controlling O<sub>2</sub> tension in the organ-on-chip

Once a specific organ-on-chip design is operational, it's often desirable to maintain the chip design even though hardware extraneous to the device may change. Therefore, our strategy was to first examine separately the O<sub>2</sub> tension in the scavenger-microfluidics separate from the microfluidic device. The main components of the scavenger-microfluidics include the tubing leading to the microfluidic device (Fig. 1C) and a scavenger-microfluidic line located on the chip.

The concentration of O<sub>2</sub> at the outlet of the scavenger tubing ( $C_{\text{out}2}$ ) is the inlet to the chip, and thus directly impacts the O<sub>2</sub> concentration in the chip. To understand how the design of tubing impacts  $C_{\text{out}2}$ , one must consider the simultaneous convection and diffusion of O<sub>2</sub> in the solution, the permeability of the tubing to O<sub>2</sub>, the chemical consumption of O<sub>2</sub> by sodium sulfite, and physical dimensions of the tube (namely, the length and the radius). These features are all captured in our mathematical framework and the three independent dimensionless groups:  $Pe_1$ ,  $Da_1$ , and  $L^\circ$ .  $Pe_1$  represents the ratio of the rate of convection of O<sub>2</sub> to diffusion of O<sub>2</sub> radially across the tube wall. In contrast,  $Da_1$  represents the ratio of the rate of O<sub>2</sub> consumption by reaction with sodium sulfite to diffusion of O<sub>2</sub> radially across the tube wall. When the mass transfer is limited by convection (low  $Pe_1$ ),  $C_{\text{out}2}$  increases with increasing  $Pe_1$ , but when the mass transfer is limited by diffusion (high  $Pe_1$ ),  $C_{\text{out}2}$  decreases with increasing  $Pe_1$  (Fig. 2A). We defined a threshold or critical value of  $Pe_1$  for

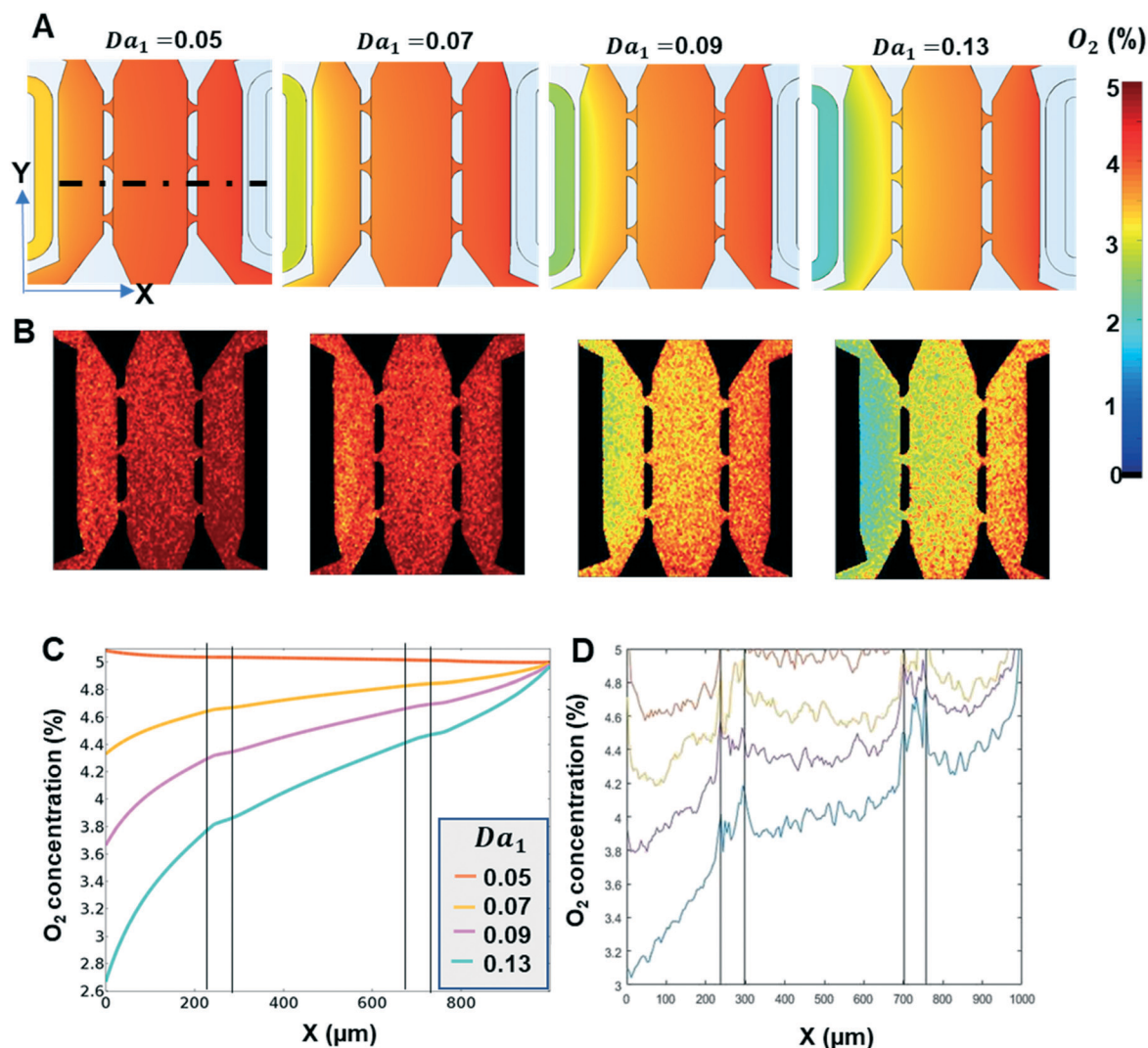


**Fig. 3** The concentration profiles of  $O_2$  in the microfluidic device can be precisely predicted. The sodium sulfite was continuously perfused through the scavenger microfluidic line and the right fluidic line was maintained at 5%  $O_2$  (see Fig. 1A). The tissue chambers were filled with ECM (without cells). The  $O_2$  concentration profiles were computed using the COMSOL and the 2D contour plots (A) and line plots (C) are shown. The line plot was along the horizontal axis (dotted line in A) in the X-direction. The  $O_2$  profiles were measured using PhLIM, and 2D contour plots (B) and line plots (D) are shown.

our system ( $Pe_{crit}$ ) that defines the separation between “high” and “low”  $Pe_1$ ; in other words, below and above which increasing  $Pe_1$  has a contrasting impact on  $C_{out2}$  (Fig. 2D) can be found by differentiation of eqn (3) and (5)–(9) to get,

$$\frac{1}{Pe_{crit}} = -\ln \left[ \frac{(y_{A1} - y_{A2}) + (S_w^\circ Da_1 - Da_1)}{(y_{A1} - Da_1)(1 + L^\circ)} \right] \quad (11)$$

The Damkohler number is directly proportional to the consumption rate of  $O_2$  so as the  $Da_1$  increases,  $C_{out2}$  decreases (Fig. 2A) and reaches zero depending on the values of the  $Pe_1$  and  $L^\circ$ . For the conditions we analyzed (Fig. 2A),  $C_{out2} \cong 0$  for  $Da_1 > 0.12$ . As  $L^\circ$  increases,  $C_{out2}$  increases. These data demonstrate that  $C_{out2}$  could be varied by changing  $Da_1$ ,  $Pe_1$ , and  $L^\circ$ .

We next examined how the design of the microfluidic device itself impacted  $O_2$  tension. To do this we used  $C_{out2}$  as the inlet boundary condition ( $C_{in3}$ ) for the simplest microfluidic device design: a single microfluidic channel (Fig. 2B) with a range of parameters that are typically used for organ on chip experiments (Table 3). These parameters corresponded to  $Pe_3$  and  $Da_3$  (defined in eqn (10)) ranges of 1.6–12 500 and 0.02–23, respectively. The COMSOL simulations demonstrate that the steady  $O_2$  spatial profiles are impacted by  $Pe_3$  and  $Da_3$  (Fig. 2C and D). In particular, the  $O_2$  concentration around the scavenger line decreases with increasing  $Pe_3$  and  $Da_3$ . However, at high  $Da_3$  ( $\geq 0.12$ ), the impact of  $Da_3$  is blunted (Fig. 2C), indicating that the  $O_2$  profiles in the device are primarily controlled by mass transfer.

Unlike the tube leading to the device, an analytical solution does not exist for the microfluidic device. Thus, to

create a simplified design equation for estimating the O<sub>2</sub> concentration in the device, we chose a single O<sub>2</sub> concentration at a point on the wall of the scavenger line ( $C_{\text{wall}}$ ) located half way into the line (5 mm from the inlet), to reduce the impact of the inlet boundary. Several standard relationships were tested by multiple linear regression and the following relationship was optimal based on the fit ( $R^2$ ) to the model data.

$$\frac{C_{\text{wall}}}{y_{\text{A2}} - C_{\text{wall}}} = \beta_0 (\text{Pe}_3)^{\beta_1} (\text{Da}_3)^{\beta_2} (C_{\text{in3}}^{\circ})^{\beta_3} \quad (12)$$

where  $C_{\text{wall}}^{\circ} = \frac{C_{\text{wall}}}{S_{\text{PDMS}}}$ ;  $C_{\text{in3}}^{\circ} = \frac{C_{\text{in3}}}{S_{\text{w}}} = \frac{C_{\text{out2}}}{S_{\text{w}}}$ .

Linear regression using the logarithmic transform of eqn (12) was used to find the constants ( $\beta_0, \beta_1, \beta_2, \beta_3$ ). As  $C_{\text{in3}}^{\circ}$  is nearly zero for  $\text{Da}_1 > 0.12$  (Fig. 2A), a separate regression was performed without the  $C_{\text{out2}}^{\circ}$  term and the values of the constants are given in Table 4. The standard error on the estimates can be found by multiplying with  $10^{\pm \text{SE}}$  (Table 4). The  $P$  values for all the coefficient of the regression were  $\ll 0.01$  and the  $R^2$  was 0.8 and 0.9 for  $\text{Da}_1 \leq 0.12$  and  $> 0.12$ , respectively (Fig. S5 and S6†). As expected,  $C_{\text{wall}}^{\circ}$  strongly correlated with the  $\text{Pe}_3$ , but was a weak function of  $\text{Da}_3$  when  $\text{Da}_1 > 0.12$  (Fig. S5 and S6† and Table 4).

### Predicting O<sub>2</sub> concentration in the device

To validate our model with measurements in our experimental microfluidic device (Fig. 1A and B), we chose to vary  $\text{Da}_1$ , by varying the sodium sulfite concentration (1, 2, 3, and 5 mM), while setting  $\text{Pe}_1 = 2.2$  and  $L^{\circ} = 1.5$ . The sodium sulfite concentrations of 1, 2, 3, and 5 mM corresponded to  $\text{Da}_1 = 0.05, 0.07, 0.09,$  and  $0.13$ , respectively. Under these conditions,  $C_{\text{out2}}$  decreases with increasing  $\text{Da}_1$  (Fig. 2A, white asterisks), and at the highest value  $\text{Da}_1$  approaches zero, or a perfect sink. Using these values for  $C_{\text{out2}}$  as the inlet concentration to the microfluidic device, the steady state O<sub>2</sub> concentration profiles were computed from the COMSOL model. Not surprisingly, the spatial concentration in the  $x$ -direction decreases with increasing  $\text{Da}_1$  (Fig. 3A and C). This prediction matched well with the experimental measurements performed using PhLIM (Fig. 3B and D). While the average concentration of O<sub>2</sub> in the hypoxia chamber was 5.0, 4.5, 4.0, and 3.2%, the average concentration in the physioxia chamber remained  $> 4.6\%$  at  $\text{Da}_1 = 0.05, 0.07, 0.09,$  and  $0.13$ , respectively (Fig. 3A). Moreover, the O<sub>2</sub> concentration gradients in the device can be varied. In particular, the hypoxia chamber experienced

concentration gradients of approximately 0, 1.2, 2.4, and 4.4%  $\text{mm}^{-1}$  for the increasing values of  $\text{Da}_1$  (Fig. 3C and D). Thus, extremely fine variations in O<sub>2</sub> concentrations and gradients could be easily produced in the device. By keeping extremely small residence time of the fluid in the microfluidic chip compared to the tubing, the O<sub>2</sub> concentration in the microfluidic device can be controlled by a single external-chip-parameter,  $C_{\text{out2}}$ .

To validate the generalized design eqn (12) for the device, the concentration of O<sub>2</sub> was computed at the left wall of the hypoxia tissue chamber (Fig. 1B), which was located 30  $\mu\text{m}$  from the scavenger line. Since eqn (12) predicts the O<sub>2</sub> concentration right at the wall of the scavenger-microfluidic line, we assumed a linear steady state concentration-increase from the scavenger-microfluidic line to the equivalent point in the experimental microfluidic device (a distance of 30  $\mu\text{m}$ ). The slope of the line was determined using the boundary condition of 5% O<sub>2</sub> in the physioxia line on the right-hand side of the device (970  $\mu\text{m}$  from the wall of the scavenger-microfluidic line). The concentrations of O<sub>2</sub> by this method were 4.8, 4.6, 4.0, and 2.1% at  $\text{Da}_1 = 0.05, 0.07, 0.09,$  and  $0.13$ , respectively. These correlation-based computations are close to the results obtained from whole chip simulations, which were 5.0, 4.3, 3.7, and 2.7% (Fig. 3C).

Next, to understand the impact of conditions in the tissue chamber, we studied effect of interstitial flow orthogonal to the O<sub>2</sub> spatial gradient and cell density in our device. The COMSOL simulations (Fig. S8†) show that the interstitial flow in the physiological range (0.5–5  $\mu\text{m s}^{-1}$ ) does not impact the O<sub>2</sub> profile. Similarly, the density of the cells, if below  $40 \times 10^6 \text{ mL}^{-1}$ , does not significantly affect the O<sub>2</sub> profile (Fig. S9†).

### HIF-1 $\alpha$ expression imparts growth advantage in breast cancer tumor cells at physioxia

We next wanted to examine the impact of O<sub>2</sub> tension in a biologically relevant system. We chose to manipulate HIF-1 $\alpha$  in a well characterized human breast cancer cell line, MDA-MB-231. HIF-1 $\alpha$  levels at 5% O<sub>2</sub> were high and co-localized with the nuclei (Fig. 4A and S7†), consistent with the stabilization of HIF-1 $\alpha$  at 5% O<sub>2</sub> compared to 20%. To examine the impact of HIF-1 $\alpha$ , we knocked down HIF-1 $\alpha$  in MDA-MB-231 cells (shHIF-1 $\alpha$ ) using shRNA. A reduced expression of HIF-1 $\alpha$  in the shHIF-1 $\alpha$  clones was observable by immunofluorescence (Fig. 4A) and confirmed by qPCR (reduced by  $> 60\%$  compared to the WT or scrambled controls, Fig. 4B). The growth of MDA-MB-231 tumors at 20% when implanted in the device was on average 1.2-fold (range of 0.9–1.6%) after four days of culture. MDA-MB-231 breast cancer cells implanted in the device showed enhanced growth and migration at 5% O<sub>2</sub> compared to 20% (Fig. 4C). The knockdown of HIF-1 $\alpha$  eliminated the enhanced growth and migration observed at 5% O<sub>2</sub> (Fig. 4C). Thus, this system provides a convenient biological model to examine the O<sub>2</sub> sensitivity of tumor cells mediated by HIF-1 $\alpha$ .

**Table 4** The constants for eqn (12) found by regression analysis

Model parameters	$\text{Da}_1 \leq 0.12$	$\text{Da}_1 > 0.12$
$\beta_0$	4.2	2.3
$\beta_1$	-0.4	-1
$\beta_2$	-0.4	-0.3
$\beta_3$	1.8	0
SE on the estimate	0.3	0.3

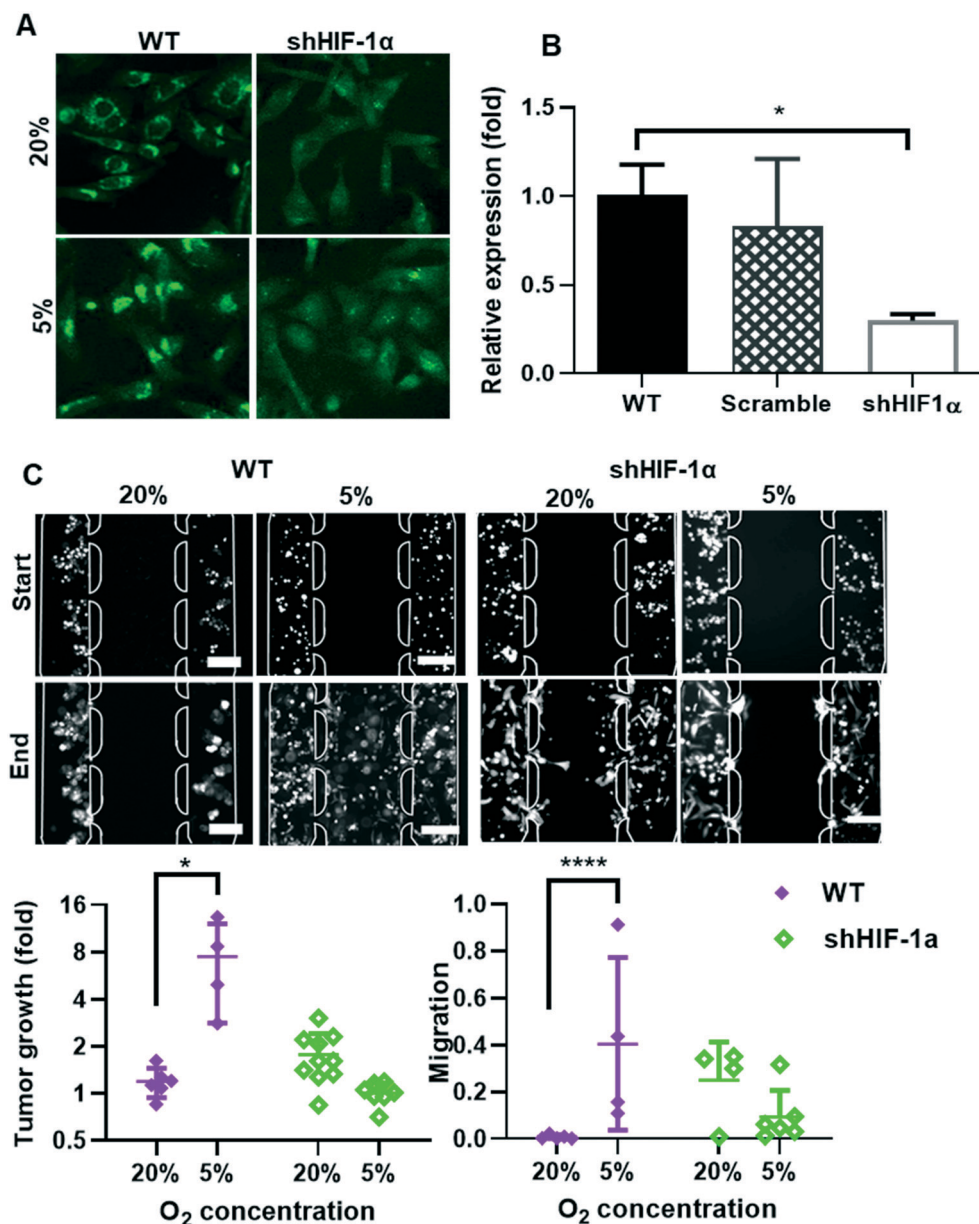
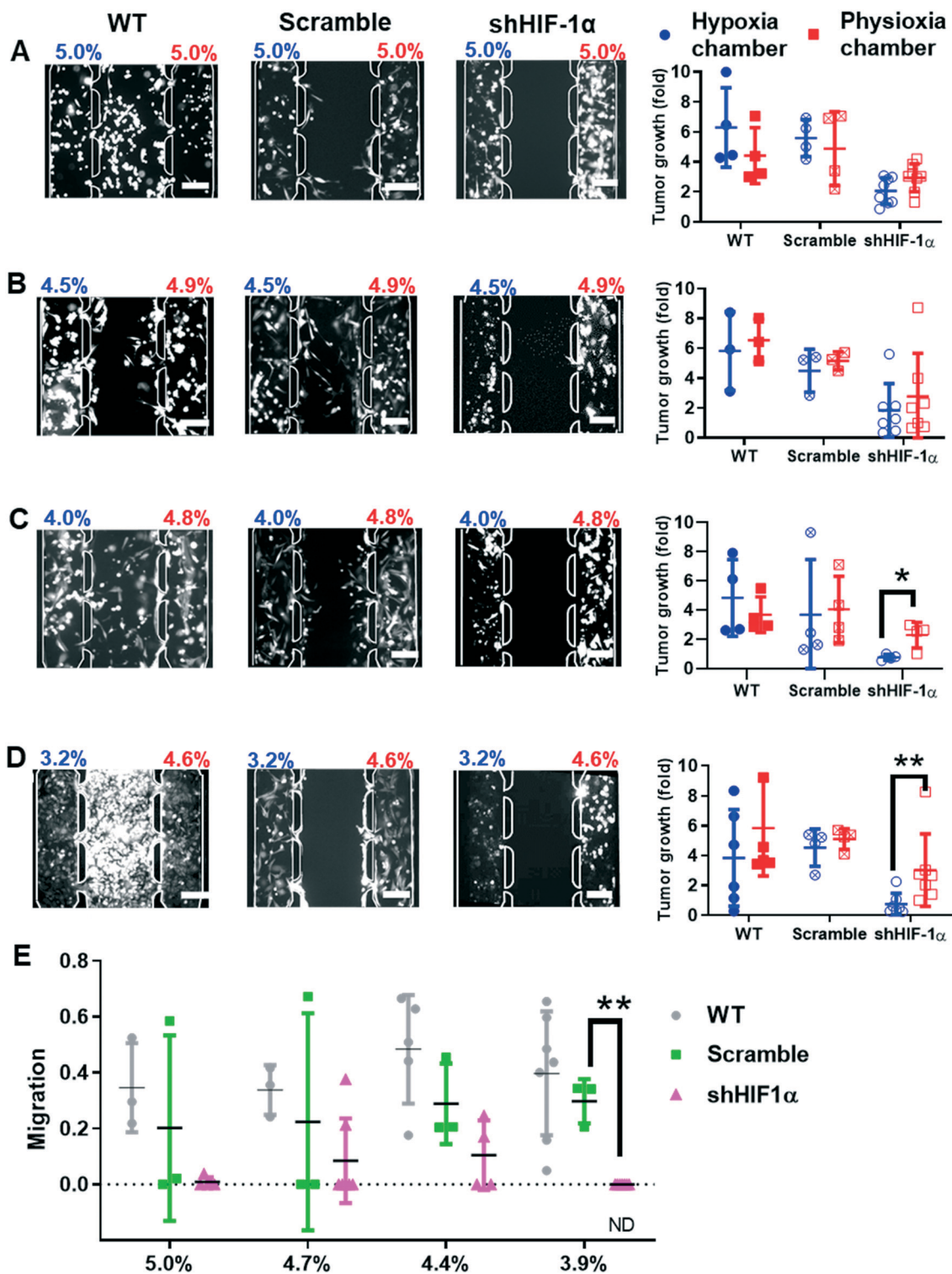


Fig. 4 Enhanced tumor proliferation and migration at 5% compared to 20% O<sub>2</sub> for control MDA-MB-231 cells. (A) WT and shHIF-1 $\alpha$  cells were analyzed for HIF-1 $\alpha$  by immunofluorescence staining. (B) qRT-PCR analysis for HIF-1 $\alpha$  gene was performed to find knockdown efficiency. The results were presented as relative expression found by 2 <sup>$\Delta\Delta$ CT</sup> method. (C) Images of representative devices acquired at the start and end of the experiment (fourth day) for indicated concentration of O<sub>2</sub>. The tumor growth (fold) was quantified by normalizing the tumor area at the end of experiment with that at the beginning and migration were quantified. \*,  $p < 0.05$ ; \*\*\*\*,  $p < 0.0001$ . Scale bar: 200  $\mu$ m.

### HIF-1 $\alpha$ expression maintains breast cancer cell growth and migration in mild chronic hypoxia

To examine the role of HIF-1 $\alpha$  in tumor growth at or just below physioxia, the WT, Scramble, and shHIF-1 $\alpha$  cells were grown under the average concentration of O<sub>2</sub> that ranged from 3.2–5.0% (Fig. 5A). The design of the device creates chronic hypoxia (hypoxia chamber) on one side while maintaining near physioxia (>4.6%, physioxia chamber) on the other side of each chip (Fig. 1B and 3A and B). The growth of Scramble and WT tumors was not affected by the

range of hypoxia examined (Fig. 5A–D). The growth of the shHIF-1 $\alpha$  tumors was not affected when the average O<sub>2</sub> concentration in a chamber was  $\geq 4.5\%$  (Fig. 5A and B). However, the growth of shHIF-1 $\alpha$  tumors maintained at mean O<sub>2</sub> concentration of 3.2% and 4.0% was significantly less compared to the growth of shHIF-1 $\alpha$  tumors in the physioxia chamber of the same chip (Fig. 5C and D). In addition to tumor growth, we measured tumor migration into the central chamber. The migration of WT and Scramble cells was not impacted by the hypoxic conditions (Fig. 5E). The migration of shHIF-1 $\alpha$  cells was significantly reduced at an



**Fig. 5** The MDA-MB-231 breast cancer cells respond to mild chronic hypoxia conditions in HIF-1 $\alpha$  dependent manner. (A–D) WT, Scramble, or shHIF-1 $\alpha$  tumors were seeded into the hypoxia and physioxia chambers of the chip. The hypoxia was introduced by flowing 1 mM (A), 2 mM (B), 3 mM (C), or 5 mM (D) sodium sulfite. The average O<sub>2</sub> concentrations in the hypoxia (blue text) and physioxia (red text) chambers are indicated. Scale bar = 200  $\mu$ m. The tumor growth (fold) was quantified by normalizing the tumor area at the end of experiment with that at the beginning. The comparison of the hypoxia chamber (blue) to the physioxia chamber (red) is shown for each condition in the plots (right panels). (E) Each of the condition in A is analyzed for tumor migration. The migration was quantified by normalizing the tumor area in the central chamber with the total tumor area in the device at the end of the experiment. The concentration of O<sub>2</sub> averaged for the entire device (all the three tissue chambers) is shown on the x-axis. \*\* is  $p < 0.01$ .

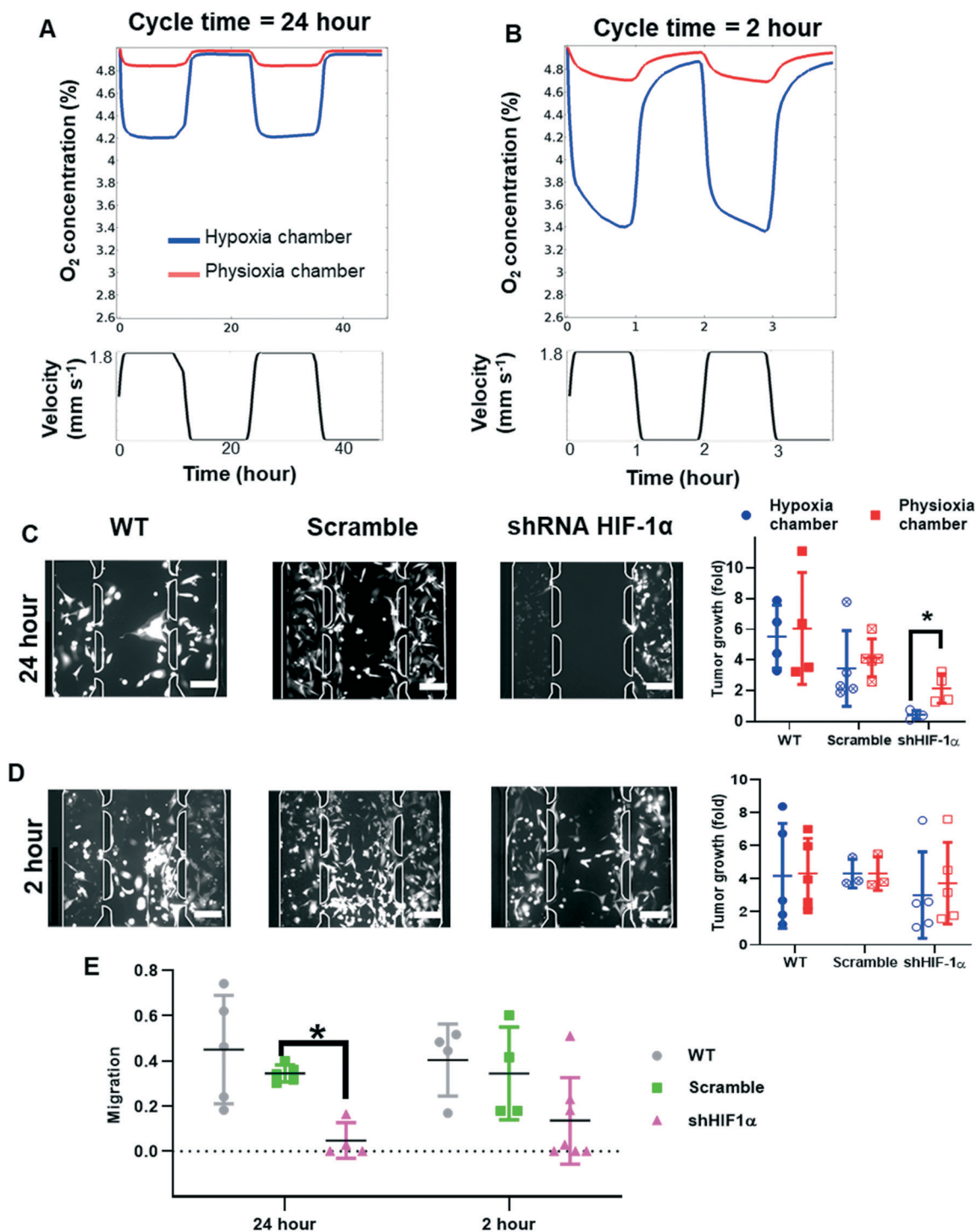


**Fig. 6** The period of intermittent hypoxia cycle impacts tumor growth in HIF-1 $\alpha$  dependent manner. (A) The intermittent hypoxia conditions were simulated, and concentration of O<sub>2</sub> was found in the hypoxia and physioxia chambers. The flow of sodium sulfite solution (3 mM) was cyclically turned on and off for a cycle time of 24 hours. The inlet velocity of the sodium sulfite solution (bottom panel) and the space averaged O<sub>2</sub> profiles (top panel) are shown. (B) The flow of sodium sulfite solution (9 mM) was cyclically turned on and off for a cycle time of 2 hours. The inlet velocity of the sodium sulfite solution (bottom panel) and O<sub>2</sub> profiles (top panel) are shown. (C and D) WT, Scramble, and shHIF-1 $\alpha$  tumor were grown under intermittent hypoxia conditions defined in A and B. Representative images at indicated cycle times are shown. Scale bar = 200  $\mu$ m. The tumor growth was quantified by normalizing the tumor area at the end of experiment with that at the beginning for both the cycle times. \*,  $p < 0.05$ . (E) The migration was quantified by normalizing the tumor area in the central chamber with the total tumor area in the device at the end of the experiment. The time on x-axis indicate the cycle time. \* is  $p < 0.05$ .

average  $O_2$  concentration of 3.9%. These data demonstrate that the expression of HIF-1 $\alpha$  plays a role in growth and migration to counter relatively mild hypoxia (3.2–4.0%) conditions.

### Temporal fluctuations in hypoxia differentially impact HIF-1 $\alpha$ -mediated functional changes

To probe the dynamics of the hypoxia response, the flow of the sodium sulfite solution was turned on and off for two different cycle times. With the flow of sodium sulfite on (period of the cycle was 24 hours and the concentration of sodium sulfite was 3 mM), the concentration of  $O_2$  in the hypoxia chamber decreased to a steady 4.2% in approximately 1 hour (Fig. 6A). When the flow of sodium sulfite was off the concentration of  $O_2$  returned to 5% in approximately 1 hour (Fig. 6A). The time and space-averaged concentration of  $O_2$  over a complete on-off cycle was  $\sim$ 4.5% in the hypoxia chamber and  $>$ 4.8% in the physioxia chamber of the device. The growth or migration of WT or Scramble tumors were not significantly different (Fig. 6C and D). However, the shHIF-1 $\alpha$  tumor growth in the hypoxia chamber, compared to the physioxia chamber, was significantly lower (Fig. 6C). The migration of the shHIF-1 $\alpha$  tumors was also significantly lower compared to the WT or Scramble controls (Fig. 6E). These results contrast to the chronic hypoxia condition with the same average concentration of 4.5%  $O_2$ , which did not impact growth or migration of the shHIF-1 $\alpha$  tumors (Fig. 5B and E).

Next, we used short 2 hours cycles but with 9 mM concentration of sodium sulfite. Under these conditions with the sodium sulfite turned on, the concentration of  $O_2$  in the hypoxia chamber decreased to 3.4% (Fig. 6B), while the time- and space-averaged concentration of  $O_2$  over a complete on-off cycle was 4.2% in the hypoxia chamber of the device. Interestingly, the growth of shHIF-1 $\alpha$  tumors in the hypoxia chamber was not different from the control tumors nor different from the shRNA tumors growth in the physioxia chamber (Fig. 6D). Similarly, the migration of the tumors did not differ with the type of cell clone or  $O_2$  concentration (Fig. 6E).

## Discussion

Tumors and many other types of diseased and non-diseased tissues experience mild hypoxia with  $O_2$  concentrations ranging from 3–5%. The hypoxic  $O_2$  concentrations are not always constant but fluctuate in both space and time because of the irregular and damaged blood supply to certain tissues, such as solid tumors. The level of hypoxia and its fluctuations under which the tumor cells are susceptible is of interest, particularly to appropriately target solid tumors. In this study, we provide quantitative design strategies to create fine temporal and spatial control of  $O_2$ . We tested the platform using MDA-MB-231 human breast cancer cells and demonstrate that changes in the steady concentration of  $O_2$  of  $\leq$ 1% can impact the proliferation and migration of breast

cancer cells. Furthermore, we demonstrate that the time-average mean concentration cannot predict the response; rather, if the duration of the hypoxia exposure is long enough (e.g., 12 hours) the cell can respond despite a regular bout of physioxia.

We first developed a generalized framework. To create mild hypoxia, we used a dilute sodium sulfite solution ( $\leq$ 5 mM) and  $O_2$  semi-permeable tubing that also transports scavenger fluid to the microfluidic device. The balance between the rates of  $O_2$  permeation and scavenging determine the  $O_2$  concentration exiting the tubing ( $C_{out2}$ ), and can be characterized using three independent dimensionless numbers ( $Pe_1$ ,  $Da_1$ , and  $L^\circ$ ; Fig. 2A). In addition, the concentration of sodium sulfite can be maintained relatively constant throughout the tubing if sodium sulfite  $\geq$ 1 mM and  $\tau <$  2000 s (Fig. S3 $\dagger$ ). While the semipermeable tubing provides an additional level of control to manipulate the inlet concentration of oxygen, one can simply set the permeability to zero if the tubing of interest is impermeable.

The exiting fluid from the tubing enters the microfluidic channel, where the actual concentration of  $O_2$  in the tissue compartments now depends on the specific design of the fluidic device (e.g., dimensions of scavenger line, scavenger flow, distance separating the tissue chamber from the scavenger line, dimensions of tissue chambers, etc.). These effects can be captured again using three dimensionless groups ( $Pe_3$ ,  $Da_3$ , and  $C_{in3}$ ). We used multiple regression to develop a simple design equation (eqn (12)) that should be applicable to a wide range of microfluidic device designs.

Of particular interest is the finding that at high enough  $Da_3$  ( $Da_3 >$  0.12 and  $Pe_3 =$  317; Fig. 2C),  $O_2$  consumption in the scavenger microfluidic line is complete, and  $O_2$  transport into the scavenger microfluidic line is strictly mass transfer limited. In other words, the  $O_2$  concentration profile within the device is controlled by the rate of mass transfer (convection in the microfluidic line and diffusion through the PDMS material). Of note, the device material should only impact the time required to achieve a steady state, and thus could have a significant impact on systems in which  $O_2$  is changing in time.

Our design framework to control oxygen tension includes the non-biological features of a typical microfluidic system. The goal was to create a broadly applicable theoretical framework to generate starting or initial  $O_2$  profiles, in particular at the boundaries. We analyzed our device to provide insights into how culture conditions in the tissue chamber itself could impact the  $O_2$  profiles in a limited context of our device design. We found that physiological interstitial flow orthogonal to the oxygen gradient and cell density ( $<$ 40  $\times$  10<sup>6</sup> cells per mL), do not significantly impact the  $O_2$  concentration profiles (Fig. S8 and S9 $\dagger$ ). Importantly, if interstitial was parallel to the oxygen gradient, there would likely be a significant impact, as we previously demonstrated examining the impact of interstitial flow on the concentration of vascular endothelial growth factor

(VEGF).<sup>21</sup> Nonetheless, the choice of cell and cell density will vary significantly between applications and the cellular O<sub>2</sub> consumption should be considered in design strategies, particularly those that involve cell dense tissues, or materials other than PDMS that are oxygen impermeable.

Our initial observation that MDA-MB-231 breast cancer cells have enhanced growth and migration in 5% compared to 20% O<sub>2</sub> suggests that these cells have adapted to create a survival advantage (growth and migration) at physioxia. Knocking down HIF-1 $\alpha$  completely abrogates this growth advantage demonstrating that enhanced HIF-1 $\alpha$  activity in MDA-MB-231 at physioxia provides a primary survival advantage that may impact breast cancer progression. This is consistent with previous reports demonstrating enhanced HIF-1 $\alpha$  protein levels at 5% O<sub>2</sub>.<sup>22</sup>

The growth of the MDA-MB-231 cells in our microfluidic device is smaller compared to 2D culture, which is in line with the general observation that cells in 3D grow slower. We note that the growth rate in microfluidic devices depends on various aspects of the culture, including density of the extracellular matrix, interstitial flow, cell seeding density, culture media, and geometry. For instance, it has previously been reported that the MDA-MB-231 cell line grew ~1.5- and 2.5-fold in 3.5 and 1.5 mg mL<sup>-1</sup> collagen, respectively, within a span of five days at 20% oxygen.<sup>23</sup> In our study, we used relatively higher density ECM (fibrin at 10 mg mL<sup>-1</sup>). It has also been reported that higher oxygen inhibits tumor growth of MDA-MB-231 (ref. 24) and other breast cancer cell lines<sup>25</sup> which is likely due to the fact that MDA-MB-231 cell line originated from a metastatic breast cancer, and is highly metastatic *in vivo*.<sup>26</sup>

To begin to understand the mechanisms that contribute to an enhanced level of HIF-1 $\alpha$ , we applied mild (3.2–5.0%) levels of constant hypoxia to MDA-MB-231 cells. Our results for chronic hypoxia show that tumor cell growth and migration was maintained in mild hypoxia. However, knocking down HIF-1 $\alpha$  decreased the proliferation and migration of MDA-MB-231 cells at O<sub>2</sub> levels <4.0% (Fig. 5C, D and E). This finding suggests that tumor cells may be uniquely dependent on HIF-1 $\alpha$  expression at mild hypoxia to maintain growth and migration.

We next employed equal cycles of scavenger flow and no flow to create intermittent hypoxic conditions that have time-averaged values of 4.5% and 4.2% in the hypoxia chamber and cycle times of 24 hours and 2 hours, respectively. Interestingly, although chronic hypoxia (4.5%) showed no detectable change in growth or migration, an intermittent hypoxic challenge with the same time-averaged value showed a significant difference in growth and migration. Under this condition, a long cycle (24 hours) of 3 mM scavenger flow followed by no flow was adequate to induce a similar response of a constant 3 mM sodium sulfite challenge. In contrast, a relatively short cycle of 1 hour of scavenger flow at 9 mM followed by no flow (average O<sub>2</sub> concentration of 4.2%), showed no significant difference despite a lower time-averaged O<sub>2</sub> concentration compared to the long cycle. These

data suggest that the cells experiencing mild O<sub>2</sub> deprivation sustained for a long period (several hours), but not extreme O<sub>2</sub> deprivation for a short period (<1 hour), activate HIF-1 $\alpha$  mediated rescuing mechanisms. This result provides some insight into the dynamics of HIF-1 $\alpha$  mediated responses of breast cancer cells. While most studies have examined the degree of hypoxia,<sup>27–29</sup> no direct link has been made to hypoxia cycle duration or magnitude.<sup>30–32</sup> In summary, our quantitative design strategies can be used in the design of a wide range of microfluidic devices for fine spatiotemporal control of O<sub>2</sub>, thus providing new opportunities to understand the dynamics of the cellular response to hypoxia.

## Conflicts of interest

There are no conflicts to declare.

## Acknowledgements

This work was supported by grants from the National Institutes of Health (UH3 TR00048, R01 CA170879, and UC4 DK104202) as well as the NSF GRFP DGE-1143954 (SFL).

## References

- 1 P. Vaupel and L. Harrison, *Oncologist*, 2004, **9**(Suppl 5), 4–9.
- 2 P. Vaupel and A. Mayer, *Cancer Metastasis Rev.*, 2007, **26**, 225–239.
- 3 A. J. Majmundar, W. J. Wong and M. C. Simon, *Mol. Cell*, 2010, **40**, 294–309.
- 4 G. L. Semenza, *Trends Pharmacol. Sci.*, 2012, **33**, 207–214.
- 5 B. H. Jiang, G. L. Semenza, C. Bauer and H. H. Marti, *Am. J. Physiol.*, 1996, **271**, C1172–C1180.
- 6 P. Vaupel, K. Schlenger, C. Knoop and M. Hockel, *Cancer Res.*, 1991, **51**, 3316–3322.
- 7 S. Matsumoto, H. Yasui, J. B. Mitchell and M. C. Krishna, *Cancer Res.*, 2010, **70**, 10019–10023.
- 8 K. Funamoto, I. K. Zervantonakis, Y. Liu, C. J. Ochs, C. Kim and R. D. Kamm, *Lab Chip*, 2012, **12**, 4855–4863.
- 9 T. Germain, M. Ansari and D. Pappas, *Anal. Chim. Acta*, 2016, **936**, 179–184.
- 10 M. D. Brennan, M. L. Rexius-Hall, L. J. Elgass and D. T. Eddington, *Lab Chip*, 2014, **14**, 4305–4318.
- 11 P. C. Thomas, S. R. Raghavan and S. P. Forry, *Anal. Chem.*, 2011, **83**, 8821–8824.
- 12 S. F. Lam, V. S. Shirure, Y. E. Chu, A. G. Soetikno and S. C. George, *PLoS One*, 2018, **13**, e0209574.
- 13 *Gas Barriers: An Introduction Basic Reference 5*, <http://www.soarnol.com/eng/solution/solution050723.html>, 2019.
- 14 T. C. Merkel, V. I. Bondar, K. Nagai, B. D. Freeman and I. Pinnau, *J. Polym. Sci. Pol. Phys.*, 2000, **38**, 415–434.
- 15 T. V. Esipova, A. Karagodov, J. Miller, D. F. Wilson, T. M. Busch and S. A. Vinogradov, *Anal. Chem.*, 2011, **83**, 8756–8765.
- 16 S. M. Ehsan and S. C. George, *Tissue Eng., Part A*, 2013, **19**, 1433–1442.
- 17 C. Yoon, K. K. Chang, J. H. Lee, W. D. Tap, C. P. Hart, M. C. Simon and S. S. Yoon, *Oncotarget*, 2016, **7**, 42844–42858.

- 18 A. Lalwani, J. Warren, D. Liuwantara, W. J. Hawthorne, P. J. O'Connell, F. J. Gonzalez, R. A. Stokes, J. Chen, D. R. Laybutt, M. E. Craig, M. M. Swarbrick, C. King and J. E. Gunton, *Cell Rep.*, 2019, **27**, 2370–2384.e2376.
- 19 H. Wei, Z. Xu, F. Liu, F. Wang, X. Wang, X. Sun and J. Li, *Tumor Biol.*, 2017, **39**, 101042831769168.
- 20 V. S. Shirure, Y. Bi, M. B. Curtis, A. Lezia, M. M. Goedegebuure, S. P. Goedegebuure, R. Aft, R. C. Fields and S. C. George, *Lab Chip*, 2018, **18**, 3687–3702.
- 21 V. S. Shirure, A. Lezia, A. Tao, L. F. Alonzo and S. C. George, *Angiogenesis*, 2017, **20**, 493–504.
- 22 W. Zhou, T. L. Dosey, T. Biechele, R. T. Moon, M. S. Horwitz and H. Ruohola-Baker, *PLoS One*, 2011, **6**, e27460.
- 23 B. J. Kim, S. Zhao, R. P. Bunaciu, A. Yen and M. Wu, *Biotechnol. Prog.*, 2015, **31**, 990–996.
- 24 K. Yttersian Sletta, M. K. Tveitaras, N. Lu, A. S. T. Engelsen, R. K. Reed, A. Garmann-Johnsen and L. Stuhr, *PLoS One*, 2017, **12**, e0183254.
- 25 E. V. Granowitz, N. Tonomura, R. M. Benson, D. M. Katz, V. Band, G. P. Makari-Judson and B. A. Osborne, *Anticancer Res.*, 2005, **25**, 3833–3842.
- 26 J. Welsh, in *Animal Models for the Study of Human Disease*, ed. P. M. Conn, Academic Press, Boston, 2013, pp. 997–1018, DOI: 10.1016/B978-0-12-415894-8.00040-3.
- 27 D. Feldser, F. Agani, N. V. Iyer, B. Pak, G. Ferreira and G. L. Semenza, *Cancer Res.*, 1999, **59**, 3915–3918.
- 28 C. C. Hudson, M. Liu, G. G. Chiang, D. M. Otterness, D. C. Loomis, F. Kaper, A. J. Giaccia and R. T. Abraham, *Mol. Cell. Biol.*, 2002, **22**, 7004–7014.
- 29 N. J. Mabweesh, D. Escuin, T. M. LaVallee, V. S. Pribluda, G. M. Swartz, M. S. Johnson, M. T. Willard, H. Zhong, J. W. Simons and P. Giannakakou, *Cancer Cell*, 2003, **3**, 363–375.
- 30 Y. J. Peng, G. Yuan, D. Ramakrishnan, S. D. Sharma, M. Bosch-Marce, G. K. Kumar, G. L. Semenza and N. R. Prabhakar, *J. Physiol.*, 2006, **577**, 705–716.
- 31 E. K. Rofstad, J. V. Gaustad, T. A. M. Egeland, B. Mathiesen and K. Galappathi, *Int. J. Cancer*, 2010, **127**, 1535–1546.
- 32 D. Verduzco, M. Lloyd, L. Xu, A. Ibrahim-Hashim, Y. Balagurunathan, R. A. Gatenby and R. J. Gillies, *PLoS One*, 2015, **10**, e0120958.